On the Nationwide Variability of Low-Level Jets Prior to Warm-season Nocturnal Rainfall in China Revealed by Radar Wind Profilers

Ning Li[a,b,c], Jianping Guo[a,d*], Xiaoran Guo[a,d], Tianmeng Chen[a,d], Zhen Zhang[a], Na Tang[a], Yifei Wang[a], Honglong Yang[d], Yongguang Zheng[c], Yongshui Zhou[e]

[a] *State Key Laboratory of Severe Weather Meteorological Science and Technology & Specialized Meteorological Support Technology Research Center, Chinese Academy of Meteorological Sciences, Beijing 100081, China*

[b] *College of Earth and Planetary Sciences, University of Chinese Academy of Sciences, Beijing 100049, China*

[c] *National Meteorological Centre, Beijing 100081, China*

[d] *CMA Field Scientific Experiment Base for Low-Altitude Economy Meteorological Support of Unmanned Aviation in Guangdong-Hong Kong-Macao Greater Bay Area, Shenzhen 518108, China*

[e] *Guizhou Meteorological Observatory, Guiyang, China*

Correspondence to:

Dr./Prof. Jianping Guo (Email: jpguocams@gmail.com)

Abstract

Nocturnal rainfall initiation is closely linked to low-level jets (LLJs), but national-scale LLJ features over China—especially their evolution preceding warm-seasonal nocturnal rainfall—remain unknown due to scarce high-resolution vertical wind observations. Here, we reveal the fine vertical structure of LLJs and their rapid evolution within 2 hours preceding the onset of nocturnal heavy rain (HR) and non-HR across four phases of rainy seasons in China during the warm season (April–October) of 2023–2024, utilizing data from a nationwide network of radar wind profilers (RWPs) in combination with surface observations and reanalysis data. Results show that nocturnal rainfall accounted for over 50% of warm-season rainfall, with 56% preceded by LLJs within 2 hours leading up to their onset. In monsoon regions, approximately 45% of nocturnal HR were LLJ-associated (LLJ_HR) and produced heavier rainfall than non-LLJ_HR events. Critically, LLJ_HR events underwent a minute-scale 'rapid reorganization' of LLJs structure, characterized by oscillatory evolution in jet height, frequency and strength. This creates favorable environment for the 'final-stage intensification' of dynamic field during the last ~30 min, where the widespread intensification of jet—coupled with significant thermodynamic instability—serves as a decisive triggering mechanism for HR. In stark contrast, LLJ_non-HR events exhibit quasi-steady or weakening dynamical trends, accompanied by an inadequate thermodynamic response that lacks such synergistic coupling. These findings demonstrate that minute-scale dynamic adjustments driven by swift evolution of the LLJ is essential for nocturnal HR, thereby providing observational constraints for regional model parameterizations and nowcasting accuracy.

Short Summary

Nighttime rainfall often links to low-level jets (LLJs), but we lack clarity on nationwide LLJ features. We here used a nationwide radar wind profiler network to study LLJ changes 2 hours before rainfall, covering China's 2023–2024 rainy seasons. 56% nighttime rainfall had LLJs. The LLJs-associated heavy rain needed a rapid adjustment of LLJs' vertical structure, especially a significant intensification within 30 minutes preceding rain. This shows the importance of LLJ in nowcasting rainfall.

1. Introduction

Forecasting nocturnal heavy rainfall (HR) and associated severe convective weather remains a major challenge in hazardous weather prediction (Davis et al., 2003; Trier et al., 2006), owing to the complexity of triggering mechanisms, the scarcity of continuous high-resolution observations, and inaccuracies in model parameterizations (Carbone and Tuttle, 2008; Reif and Bluestein, 2017; Weckwerth et al., 2019; Zhao et al., 2025). Crucially, the low-level jet (LLJ) that exhibit a diurnal cycle with a maximum at night is widely recognized as a key contributor to nocturnal HR (Bonner 1968; Mitchell et al., 1995; Tuttle and Davis, 2006), as documented in regions or countries such as the Great Plains of the United States (Maddox, 1983; Higgins et al., 1997), Argentina (Marengo et al., 2004), India (Monaghan et al., 2010), North China Plain (Li et al., 2024).

The LLJs primarily originate from the inertial oscillations (IO) following the sudden decay of turbulence after sunset (Blackadar, 1957) and thermal imbalances induced baroclinicity over sloping terrain (Holton, 1967). Functioning as concentrated corridors for heat, moisture, and momentum transport, LLJs can modulate the diurnal oscillation in water vapor by IO (Rasmusson, 1967; Zhang et al., 2019) and enhance convective instability, particularly when elevated high-θ_e air encounters frontal boundaries (Trier et al., 2017). Also, strong low-level vertical wind shear (VWS) associated with LLJs necessarily benefits deep lifting (Maddox et al., 1979; Stensrud, 1996; Rasmussen and Houze, 2016). These mechanisms collectively provide essential thermodynamic and dynamic support for the initiation and organization of nocturnal convection, especially where LLJs force low-level ascent at jet termini or via positive vorticity advection left of the jet axis (Chen et al., 2017; Du and Chen, 2019; Xia and Zhao, 2009).

Furthermore, LLJs interact synergistically with other key factors to trigger HR that is associated with mesoscale convective systems (Chen et al. 2010; Chen et al., 2017; Chen et al., 2024), including terrain effects (Anthes et al., 1982; Pan and Chen, 2019; Huang et al., 2020), gravity waves (Weckwerth & Wakimoto, 1992), among others.

These interactions are highly sensitive to the prevailing synoptic and subsynoptic-scale environmental conditions (e.g., Hodges and Pu, 2019) and fine-scale structural of LLJs, including LLJ frequency, spatial redistribution, and particularly localized wind profile accelerations (Pitchford and London, 1962; Walters and Winkler, 2008; Du and Chen, 2019; Li et al., 2024). Understanding these intricate evolution features of LLJs is critical for improving the forecasting of nocturnal HR.

Despite advances facilitated by regional reanalysis (e.g., Doubler et al., 2015; Li et al., 2021), numerical modeling (e.g., Zhang and Meng, 2019), radiosonde observations (e.g., Whiteman et al., 1997; Yan et al., 2020), and emerging artificial intelligence techniques (e.g., Subrahmanyam et al., 2024) in understanding the climatology and physical mechanisms of LLJs and their role in HR forecasting, significant knowledge gaps remain. A critical shortcoming lies in the inability to capture minute-scale evolution of LLJs during the nocturnal pre-storm period. Conventional observing systems lack the spatiotemporal resolution required to resolve rapid changes in pre-storm environments (Weisman et al., 2015; Cao et at., 2025; Roots et al., 2025), thereby hindering systematic analysis of fine-scale structure of LLJs and their evolution within the critical 2-hour window preceding rainfall.

Moreover, the mechanisms and impacts of LLJs exhibit considerable variation across monsoon phases and geographic regions. As a classic monsoon climate region, China exhibits particularly prominent nocturnal rainfall contributions across major climate-sensitive areas (Yu et al., 2014), where LLJs play a crucial role in modulating primary rainfall belts (Sun, 1986; Chen et al., 2010; Wang et al., 2013; Horinouchi et al., 2019), such as those in Eastern China (Chen et al., 2017; Xue et al., 2018) and South China (Du et al., 2020; Bai et al., 2021; Fu et al., 2021). However, nationwide comparative studies examining LLJ precursor signals across different monsoon phases in China are still lacking.

Radar wind profilers (RWPs) can offer transformative potential by capturing minute-resolution wind profiles to reveal pre-rainfall dynamic precursors (Zamora et al., 1987; Du et al., 2012; Molod et al., 2019; Guo et al., 2023). For example, Gebauer

et al. (2018) demonstrated the capability of RWPs to elucidate how heterogeneous structures of LLJ trigger nocturnal convection in Great Plains; Based on a linear net of RWPs deployed across the North China Plain, our previous study (Li et al., 2024) observed rapid intensification of moisture flux convergence (MFC) driven by a surge in LLJs profile within 30 min preceding nocturnal rainfall onset, highlighting the sensitivity of RWP to minute-scale perturbations of LLJs profiles. However, it remains an open question whether this minute-scale precursor is universally applicable across diverse monsoon phases throughout mainland China. Furthermore, the systematic differences in the fine-scale LLJ evolution that distinguish HR from non-HR have yet to be fully elucidated.

Therefore, this study utilizes a nationwide network of RWPs to address the following two questions: 1) How do the vertical structure of LLJs and their minute-scale evolution within 0–2 hours preceding nocturnal rainfall vary across different rainy season phases? and 2) What are the systematic differences in LLJ dynamic-thermodynamic mechanisms between LLJ-influenced HR and non-HR events? The remainder of this paper is structured as follows: Section 2 details data and methodology, Section 3 presents comparative analyses of characteristics of rainfall and LLJs evolution, and Section 4 synthesizes key conclusions.

2. Data and Methodology

2.1 Radar wind profiler measurements

The RWP observations collected from 31 stations across China (Fig.1) from April to October in 2023–2024 were analyzed in this study, which can provide wind speed and direction with a vertical resolution of 120 m and an interval of 6 minutes (Liu et al., 2019). To reduce the potential influence of poor data quality, RWP data underwent strict quality control following procedures proposed by Wei et al. (2014) and Miao et al. (2018). Firstly, to minimize contamination from precipitation particles, which can introduce significant errors in Doppler-based wind retrieval, all observations during

rainfall periods were removed. Secondly, within each profile below 3 km above ground level (AGL), missing values and significant outliers that defined as values exceeding 2.5 standard deviations from the mean were removed. Next, for each profile, if more than 40% of the data points below 3 km AGL were outliers or missing, that entire profile was discarded. Finally, discontinuous, or missing data points were estimated using linear interpolation. Following this quality control process, 109,400 wind profiles were discarded and a total of 2,606,042 profiles across China were available for analysis during the study period.

2.2 Multi-source meteorological data

In addition, 1-min rainfall measurements were directly acquired from the rain gauge measurements at 2160 national weather stations across China to identify rainfall events. Rainfall amounts were accumulated over 6-min intervals to ensure temporal alignment with the RWP measurements. Ground-based meteorological variables are measured at 1-min intervals from national weather stations, including 2-m air temperature, relative humidity, and surface pressure. All ground-based data have undergone rigorous quality control (China Meteorological Administration, 2020; Zhao et al., 2024) and are publicly accessible at the National Meteorological Information Center of China Meteorological Administration (CMA).

Furthermore, to diagnose large-scale circulation patterns and environmental conditions preceding nocturnal rainfall influenced by LLJs, this study utilized meteorological variables derived from the fifth generation of the European Centre for Medium-Range Weather Forecasts atmospheric reanalysis (ERA5) of the global climate (Hersbach et al., 2020). The ERA5 data features a horizontal resolution of 0.25°×0.25° across 37 vertical pressure levels and hourly temporal resolution. Unless otherwise specified, all datasets cover the study period of April to October in 2023–2024.

2.3 Identification of nocturnal rainfall events

Firstly, days with typhoon activity were excluded. To minimize the impact of rainfall on RWP measurements, a minimum dry interval of 2 hours was required between consecutive rainfall events. Following the methodology of Li et al. (2024), a rainfall occurrence was defined when the total accumulated rainfall which was measured by all rain gauges within a 25-km radius of each RWP station exceeded 0.1 mm. Accounting for rainfall intermittency, a valid rainfall event required at least two subsequent occurrences within 30 min following initial detection. Any isolated initial occurrence not meeting this criterion was discarded. Notably, this 25-km radius serves as a rigorous spatial constraint to not only mitigates the limitations of single-gauge measurements but also ensures the onset of rainfall at this scale are temporally coherent with that of the rain gauge co-located with RWP (as confirmed by sensitivity tests in Fig. S1). This guarantees direct physical coupling between local rainfall and the RWP-observed wind profiles.

Nocturnal rainfall events were defined as those occurring between 2000 and 0800 Local Standard Time (LST). Based on operational classifications from the National Water Resources Bureau and CMA, the rainy season was categorized into four consecutive phases: (1) the South China Pre-summer Rainy Season (April 1 to June 8, 2023 and April 1 to June 9, 2024), (2) the Meiyu Season (June 9 to July 14, 2023 and June 10 to July 21, 2024), (3) the North China Rainy Season (July 15 to August 31, 2023 and July 22 to August 31, 2024), and (4) the West China Autumn Rainy Season (September 1 to October 31 for both 2023 and 2024). These phases are subsequently designated as Phase 1 to Phase 4 throughout this study. Four regions of interest (ROIs) were subsequently selected for detailed analysis (see Table 1).

Further screening identified locally nocturnal HR events, where the mean 6-min rainfall intensity exceeded the 75th percentile of all recorded rainfall events at each station. This threshold can effectively distinguish significant HR from weak rainfall while ensuring a sufficient sample size for robust statistical analysis of minute-scale LLJ dynamics (Table S1). Furthermore, a sensitivity test by varying the thresholds to

85th and 95th percentile to ensure that the main conclusion regarding the precursory signals of LLJs is robust within a reasonable threshold range (see Figs. S2–S5),.

Statistical analysis revealed 3,155 nocturnal rainfall events during the 2023–2024 warm seasons (within the 31 red circles shown in Fig.1). Event counts per rainy season phase were 1,109, 689, 652, and 705 respectively, with 841 events classified as nocturnal HR events.

2.4 Identification of LLJs and associated rainfall event

To ensure identified LLJs exhibit significant vertical wind shear characteristic of jet-like profiles, the following criteria are adopted: (1) a maximum horizontal wind speed exceeding 10 m s^{-1} in the lowest 3 km AGL, and (2) a wind speed reduction of at least 3 m s^{-1} from the maximum to minimum below 3 km AGL, or to 3 km AGL if no minimum exists. These deliberately conservative wind speed thresholds maximize LLJ sample size for enhanced statistical robustness. This definition standard has been widely adopted in previous studies (Bonner, 1968; Whiteman et al., 1997; Du et al., 2014; Yan et al., 2020). The strength of LLJ or jet nose is defined as the maximum wind speed along the entire profile. The LLJ core height is defined as the altitude of the wind speed maximum during LLJ occurrences. Correspondingly, the LLJ direction is determined by the wind direction at the height of the LLJ.

We define rainfall events where LLJ occurs at least twice within 2 hours before rainfall as an LLJ event (Li et al., 2024). The HR events influenced by LLJs (LLJ_HR events), HR events without LLJ influence (non-LLJ_HR events), and non-HR events affected by LLJ (LLJ_non-HR events) are further distinguished.

3. Results and discussion

3.1 General characteristics of nocturnal rainfall and LLJs

Firstly, we characterized the spatiotemporal patterns of rainfall and LLJs observed nationwide during the 2023-2024 warm season. Nationally, nocturnal rainfall accounted for 50.9% of total warm-season rainfall, with pronounced concentrations

over North, Northeast and Southwest China (Figs. 2d and 2g). In contrast, the pronounced daytime rainfall dominance in South China (Fig. 2a) may arise from the interaction between enhanced onshore monsoonal flows and terrain (Bai et al., 2020), sea breeze fronts and cold pool (Chen et al., 2016). In terms of frequency, nocturnal rainfall occurred more frequent, constituting 52.5% of the total rainfall frequency versus 47.5% for the daytime, with the highest nocturnal proportions found in southwestern and eastern regions (Figs. 2e and 2h). Although the national mean rainfall intensity was generally lower at night (1.2 mm/h) than during the day (1.2 mm/h; Figs. 2c and 2f), the probability of nocturnal HR occurrence was was significant (51.3%), particularly across western China, North China, and northeastern China (Fig. 2i).

Figure 3 displays the key attributes of LLJs detected at all 31 RWPs across China using the criteria defined in Section 2. Nocturnal LLJs activities occurred more frequently, with an overall occurrence frequency increase of nearly 18% (Figs. 3a and 3e). Spatially, the regions exhibiting pronounced jet activity and high absolute wind speeds were collocated with those experiencing intense nocturnal rainfall, particularly over northern and eastern regions. Vertically, these jets manifest as intensified LLJ core concentrated below 1 km AGL (Figs. 3f and 3g). This vertical restructuring likely responds to nocturnal surface cooling and IO. The dominant wind direction shifted to westerly, southerly or southwesterly flows at night across most regions, potentially driven by thermal contrasts within the monsoon circulation pattern and topographic forcing.

Statistical analysis revealed substantial linkage between LLJs and nocturnal rainfall. Specifically, 56% of nocturnal rainfall events across China were preceded by the presence of LLJs within 2 hours, establishing nocturnal rainfall influenced by LLJs as a major component of warm-season rainfall in China. This relationship was modulated by the seasonal migration of the western Pacific subtropical high (WPSH), which drove corresponding shifts in HR belts that closely synchronized with the spatiotemporal evolution of LLJ activity. The proportion of nocturnal rainfall events associated with LLJs during the four rainy season phases reached 60.4%, 56.3%, 49.4%,

and 54.9%, respectively (Fig. 4a). Among 841 identified nocturnal HR events, the percentages classified as LLJ_HR events ranged from 33.9% to 47.2% across the four phases. These results indicated that the mere presence of LLJs, while a frequent precursor to general nocturnal rainfall, is necessary but insufficient for HR.

However, spatial analysis of site-averaged rainfall intensity revealed that LLJ_HR events consistently produced heavier rainfall than non-LLJ_HR events, particularly within the four ROIs identified in each phase (red boxes in Fig. 5). The non-LLJ_HR events exhibited spatially heterogeneous intensity distributions, where localized maxima may occur in areas outside the primary rain belts. For instance, during Phase 2 in ROI-3 (Fig. 5f), sporadic high-intensity events driven by deep cold trough system resulted in high site-averaged intensities even without LLJs, whereas in ROI-2, the absence of LLJs typically corresponded to weaker frontal precipitation (Fig. S6). This reflected the dominant role of LLJ coupling in primary rain belts region. Furthermore, a total of 71, 49, 33, and 34 nocturnal HR events were identified in these ROIs during from Phase 1 to Phase 4 (Fig. 4b). From the LLJs perspective, nearly 31.1% of LLJ events were classified as HR events across phases relative to LLJ_non-HR events, which unexpectedly suggests the presences of LLJs do not invariably result in HR. From the HR perspective, nearly 45.0% of HR events were associated with LLJs within 2 hours before onset relative to non-LLJ_HR events. In general, these findings imply an association between HR and LLJ in ROIs during specific phases, but certain HR instances can still materialize during non-LLJ events due to other influencing factors (e.g., land-sea breezes, topographic lifting, or mesoscale convective systems).

Furthermore, at the national scale, probability distributions of rainfall intensity (Fig. 6) indicated that LLJ_HR events exhibited a distinct probability advantage in the high-intensity tail (≥ 2 mm/6 min) compared to non-LLJ_HR events during Phases 1 and 3. During Phases 2 and 4, however, the distributions of the two event types were similar, and LLJ_HR events even exhibited somewhat weaker rainfall. Regionally, rainfall intensities within the key ROIs generally exceeded the national average, particularly for LLJ_HR events. Specifically, LLJ_HR events in ROI-1 and ROI-2

demonstrated significantly higher probabilities of heavier rainfall (≥ 2 mm/6 min), while those in ROI-4 during Phase 4 favored intensities near 0.5 and 2.8 mm/6 min. Notably, despite the relatively high frequency of LLJ_HR events in ROI-3 during Phase 3 (see the pie charts in Fig. 6), their probability of producing extreme rainfall intensities was lower than that of non-LLJ_HR events. This suggests that LLJs may not represent the dominant mechanism for extreme rainfall in this particular region and season.

In summary, although LLJ_HR events generally exhibit higher rainfall intensities, the relatively high proportion of LLJ_non-HR events suggests that the mere presences of LLJs does not invariably lead to HR. Therefore, further investigating the fine-scale vertical structures of LLJs preceding rainfall is crucial to distinguish the specific dynamical characteristics of LLJs that lead to HR.

3.2 Minute-scale evolution of LLJs preceding nocturnal heavy and non-heavy rainfall

To elucidate the contrasting precursor characteristics of LLJs that lead to nocturnal rainfall of differing intensities, this section examines fine-scale vertical structure and continuous evolution of LLJs within 2 hours preceding both LLJ_HR and LLJ_non-HR events during four phases in their respective ROIs. The results revealed the distinct spatiotemporal variations in vertical structure and evolutionary patterns of LLJs occurred across seasonal phases.

During Phase1 in ROI-1, LLJ_HR events exhibited a significant increase in frequency starting 108 min before rainfall onset, reaching secondary peaks at –84 min and –60 min, culminating in maximum frequency immediately preceding HR (Fig. 7a). Meanwhile, the average wind profiles showed a rapid intensify trend from 48 min before HR onset, with the jet core reaching its peak wind speed (about 12.2 m s^{-1}) and its height distinctly decreased (Fig. 8a), although there is the transient weakening of jet strength within 60–48 min preceding HR. These LLJs featured a bimodal vertical distribution with frequent occurrence layers at 0.5–1 km and 1.5–2 km AGL. This structure was characteristic of double low-level jets (DLLJs), where the coexistence of the boundary layer jets (BLJs) and synoptic-system-related low-level lets (SLLJs)

generates a deep layer of forced ascent via BLJ-exit convergence and SLLJ-entrance divergence. This dynamical coupling significantly favors organized deep convection in ROI-1 (Uccellini and Johnson, 1979; Du and Chen, 2018; Du and Chen, 2019; Liu et al., 2020). Note that the composite wind profile (Fig. 8a) does not show a distinct bimodal vertical distribution due to smoothing from averaging. Detailed examination of wind profiles revealed that approximately 40% of LLJ_HR events exhibited DLLJs, while only 20% of LLJ_non-HR events showed such a structure. Therefore, LLJ_non-HR events lacked this dynamic coupling, with jets predominantly confined to the single 0.5–1 km layer. Although LLJ_non-HR events showed a gradual increase in frequency from –48 min, along with strengthening winds prior to rainfall (Figs. 7e and 8e), these changes were rather limited compared to the pronounced evolution seen in LLJ_HR events under a background of overall lower frequency and weaker intensity. This steady and weak dynamical structure failed to provide sufficient dynamic lifting to efficiently initiate strong convection.

Both event types exhibited notably high frequencies and intensities of LLJs over ROI-2 during Phase 2, yet their evolutionary dynamics diverged sharply. For LLJ_HR events, a coherent oscillatory vertical reorganization of LLJs is evident (Figs. 7b and 8b). At the first stage, both LLJ frequency and wind speed maximum peaked (exceeding 12 m s^{-1}) at –120 min, with the core situated 1.5–2 km AGL. Subsequently, a rapid descent of frequently occurring height of LLJs to below 1 km AGL occurred, accompanied by a concurrent decline in frequency and profile intensity to a minimum around 84–72 min preceding HR. Analysis of wind kinetic energy and its vertical transport (see Eqs. 1 and 2 in supporting material) confirmed that the 'sudden drop' likely results from the downward momentum transfer (Fig. S7a and c), which can efficiently enhance low-level disturbances and dynamic forcing and serve as an effective indicator of HR 1–2 hours later (Liu et al. 2003; Fu et al., 2020). Following this descent, a distinct recovery phase ensued from –60 min, where the frequency increased reaching a secondary peak at –48 min and jet core re-ascended to 1–2 km AGL. The LLJ profile strength re-intensified to about 11.4 m s^{-1}. This rise of the jet core and secondary enhancement are likely tied to cold pool-LLJ interactions and

intensified upward motion or latent heat release in convective clouds (further discussed in Section 3.3). In conclusion, this pattern suggests an intense internal dynamical adjustment process. In comparison, LLJ_non-HR events lacked such low-level momentum transfer signals (Fig. S7b and d) and maintained a quasi-steady state, with consistent LLJs strength (near 11.8 m s^{-1}) and a preferred height range of 1–2 km AGL (Fig. 8f). The LLJs frequency exhibited gradual changes, peaking weakly at 36 min preceding rainfall before a subsequent rapid decrease (Fig. 7f). This pattern indicates an absence of the rapid dynamical redistribution observed in LLJ_non-HR events.

During Phase 3 in ROI-3, LLJ_HR events exhibited a bimodal temporal distribution in LLJ frequency, with prominent peaks at –96 min and –48 min (Fig. 7c). The dominant LLJ height was centered between 1–1.5 km AGL. The wind profiles showed a corresponding evolution where the maximum wind speed increased from approximately 8 m s^{-1} at –120 min to a first peak about 9.5 m s^{-1} by –84 min. It then reached a secondary peak near -48 min and displayed a characteristic transient weakening (–48 to –24 min), after which a rapid intensification resumed until HR occurred (Fig. 8c) Conversely, LLJ_non-HR events were characterized by substantially lower LLJs frequency (around 20%) and more diffuse structure (Fig. 7g), with wind profiles showing weaker intensification preceding rainfall (Fig. 8g). Thus, the pronounced, rapid change and final intensification in LLJs likely reflect a key dynamical mechanism conducive to HR initiation. However, the overall weaker wind profiles potentially explained the lower probability of heavier rainfall in LLJ_HR events over ROI-3 during Phase 3 relative to other region and phases.

During Phase 4 in ROI-4, LLJ_HR events exhibited a distinctive two-stage intensification process. The wind profiles initially strengthened rapidly starting from -120 min, reaching a primary peak of approximately 12.8 m s^{-1} at –72 min (Fig. 8d), coinciding with a secondary peak in LLJ frequency. Following a brief weakening (–60 to –48 min), a renewed and explosive intensification occurred from –48 min onwards, continuing until rainfall onset. Throughout this period, the LLJ cores remained concentrated between 0.5–1.5 km AGL (Fig. 7d). In sharp contrast, LLJ_non-HR events displayed a pattern of premature peaking followed by decay. Both frequency and

intensity peaked earlier at –84 min, followed by general attenuation (Fig. 7h). By –48 min, weakened wind profiles stabilized into a double-core structure maintaining around 10 m s^{-1}, with distinct jet cores near 0.8 km and 1.7 km AGL (Fig. 8h). Crucially, in the LLJ_non-HR event, this premature peak and the subsequent continuous attenuation of the low-level wind field resulted in a lack of sustained dynamic forcing during the critical pre-rainstorm stage, failing to trigger HR.

Synthesizing the evolution across all phases, although a distinct transient weakening of jet profiles was consistently observed, the wind profiles of LLJs consistently showed a rapid increasing and height of core decreased in around the final 30 min before HR. We propose that this minute-scale oscillatory behavior—characterized by a 'weakening-then-strengthening' or 'descent-then-ascent' pattern—represents a physically consistent signature of the dynamic environment adjustment essential for HR. Physically, this phenomenon is likely attributable to the momentum consumption by developing convection or the flow blocking effect due to strong convergence (Markowski & Richardson, 2010). Consequently, this rapid reorganization and final-stage intensification of the low-level dynamical field constitutes a decisive triggering mechanism for HR, standing in sharp contrast to the weaker, quasi-steady evolution observed in LLJ_non-HR events.

Furthermore, probability distributions of LLJ strength and height within 2 hours preceding rainfall were compared across key regions (Fig. 9). During Phase 1 in ROI-1, the strength of LLJs in LLJ_HR events was notably stronger by 2–3 m s^{-1} than that in LLJ_non-HR events (Fig. 9a). Height distributions showed distinct bimodal peaks near 0.9 km and 1.75 km AGL (Fig. 9e). The average LLJs height was generally higher in LLJ_HR events, which is usually affected by the coupling of the upper-level jet stream or the sea-land breeze. During Phase 2 in ROI-2, LLJ_HR events showed higher probabilities of strong LLJs (17–28 m s^{-1}) compared to the dominant 13 m s^{-1} intensity in LLJ_non-HR events (Fig. 9b). Influenced by large-scale circulation patterns, both event types featured LLJs centered near 1.5 km AGL (Fig. 9f), though LLJ_HR events developed a secondary maximum near 0.8 km AGL due to pre-rainfall descent of the jet core (Fig. 7b). Contrastingly, Figure 9c shows that LLJ_HR events were associated

with weaker jet strengths (around 11 m s^{-1}) compared to LLJ_non-HR events (14–23 m s^{-1}) in ROI-3 during Phase 3, suggesting that strong LLJs don't necessarily induce HR here. The height of LLJ in LLJ_HR events mainly concentrated near 1.2 km AGL, whereas in LLJ_non-HR events, it was more uniformly distributed between 0–3 km AGL with a higher probability nearly 1.5 km (Fig. 9g). For Phase 4 in ROI-4, LLJs strength peaked near 15 m s^{-1} in both event types, but LLJ_HR events featured stronger jets reaching 25–30 m s^{-1} (Fig. 9d). The LLJs height in both events peaked predominantly at 0.8 km AGL, with secondary peaks at 1.5 km for LLJ_HR and 2.0 km AGL for LLJ_non-HR events (Fig. 9h).

In summary, although different internal dynamic adjustments, including frequency, occurrence height, and wind profile intensity of LLJs, preceding LLJ_HR events were observed due to the different dominant mechanisms influencing rainfall in each phase, our findings highlight the role of fine-scale LLJ structures and their rapid vertical reorganization in modulating nocturnal rainfall intensity, offering valuable insights for improving regional nocturnal HR forecasting.

3.3 Thermodynamic evolution associated with LLJs preceding nocturnal heavy and non-heavy Rainfall

The section 3.2 has clarified that the fine-scale dynamic characteristics of LLJs—including their temporal evolution, vertical structure, and intensity variations—play a pivotal role in modulating nocturnal rainfall intensity during rainy season phases. However, the influence of LLJs on rainfall generation and intensification rarely operates in isolation; instead, it depends strongly on the accompanying large-scale thermodynamic environment, which provides the necessary moisture supply and convective instability to sustain or amplify heavy rainfall. Thus, to fully unravel the mechanisms underlying the distinction between LLJ_HR and LLJ_non-HR events, it is essential to complement the dynamic analysis with an in-depth examination of the thermodynamic conditions associated with LLJs within the immediate pre-convective environment (within 1-hour preceding rainfall).

Further analysis of the large-scale thermodynamic conditions at 1 hour prior to rainfall onset (Figs. 10 and 11) reveals consistently stronger thermal instability for LLJ_HR versus LLJ_non-HR events, accompanied by stronger MFC within key regions during each rainy season.

During Phase 1 in ROI-1, thermodynamic conditions were comparable between event types. Southwesterly LLJs transported warm-moist air masses from the South China Sea and Bay of Bengal, forming a pronounced warm-humid tongue (Fig. 10a and 10e). Coupled with MFC centers developing north of the jet axis (Fig. 11a and 11e), this configuration facilitated nocturnal rainfall development. During Phase 2 in ROI-2, LLJ_HR events exhibited a significantly stronger warm-moisture tongue with core θ_e reaching 358 K—approximately 2 K higher than in non-HR events (Figs. 10b and 10f). Dynamically, the stronger LLJ core (>1.2 $m\ s^{-1}$ difference) drove a sharper, continuous band of MFC along the left flank of the jet axis (Fig. 11b), creating a robust triggering mechanism for HR (Fig. 11b). During Phase 3 in ROI-3, intensified southwesterly LLJs in HR events drove substantial northward transport of abundant moisture and higher θ_e air (>2 K difference) northward into a low θ_e environment (Fig. 10c), enhancing convective instability. The synergistic interaction of this moist, high-energy advection with orographic forcing from the Taihang Mountains generated intense MFC, with peak values south of Beijing approximately 30×10^{-5} $km\ m^{-2}\ s^{-1}$ (Fig. 11c) than those in LLJ_non-HR events, thereby driving nocturnal HR. Thermodynamic contrasts were most pronounced during Phase 4 in ROI-4. Thermodynamic contrasts were most pronounced during Phase 4 in ROI-4. LLJ_HR events featured a deep high-θ_e region (>356 K) over the southeastern Tibetan Plateau (Fig. 10d), contrasting with the cold highs and lower θ_e prevalent in LLJ_non-HR events (Fig. 10h). Concurrently, accelerated easterly-southeasterly LLJs drove warm, moist air towards the steep eastern Plateau margin. The impingement of this flow against the sharp topographic gradient generated intense dynamic lifting and low-level convergence. This mechanically forced ascent, synergizing with the abundant moisture transport and strong MFC (Fig. 11h), played an essential role in triggering the observed nocturnal HR in this region.

To elucidate the rapid processes leading to occurrence of rainfall, the minute-scale evolution of key thermodynamic and dynamic parameters was further analyzed (Fig. 12), including surface θ_e, LLJ index and VWS. Specifically, LLJ index is defined as the ratio of maximum wind speed below 3 km to the height where wind first exceeds 10 m s^{-1}.. A rapid rise in LLJ index will reflect the extension and pulsing intensity of the LLJ, and its magnitude has been shown to be positively correlated with subsequent rainfall intensity 1–2 hour later (Liu et al., 2003). VWS is calculated as the wind speed difference between the surface and jet height divided by the jet height and is used to characterize the bulk shear from the surface to the jet layer associated with the dynamical forcing and organization of convection (Wei et al., 2014).

Figure 12a illustrates that during Phase 1 in ROI-1, despite the similarity in large-scale environments between LLJ_HR and LLJ_non-HR events, they exhibited distinct differences in the continuous evolution of LLJ-associated thermodynamic conditions preceding rainfall onset. LLJ_HR events exhibited abrupt thermodynamic enhancement from 90 min preceding the onset of rainfall driven by rapid intensification of LLJs, with surface θ_e and VWS surging approximately 1.5 K and 0.5 s^{-1}respectively. Concurrently, the LLJ index surged from approximately 0.05 to 0.08 and VWS peaked sharply at -60 min, signaling LLJs intensification and core descent (Figs. 7a, 8a). This rapid, minute-scale co-intensification of thermodynamic and dynamic processes serves as a critical precursor triggering HR. In contrast, LLJ_non-HR events showed weaker increases of θ_e and VWS and a declining LLJ index (by about 0.02) alongside rising jet cores, reducing low-level shear and convergence efficiency, thereby diminishing overall rainfall intensity.

During Phase 2 in ROI-2, the thermodynamic environment displayed a distinct ‘weakening-reintensification’ pattern (Fig. 12b), which aligns precisely with the intrinsic dynamical adjustments of the wind field presented in Fig. 8b. Initially, at -120 min, concurrent peaks in the LLJ index and VWS were observed, coupled with a high surface θ_e of 348.3 K. During the subsequent transition period, a drastic elevation in the jet core height starting from -84 min caused a precipitous drop in the LLJ index. The timing of this rapid evolution suggests a transient optimal window for nocturnal rainfall

triggering that is characteristic of LLJ_HR events in ROI-2. Following this, rapid surface cooling began 60 min prior to HR. This cooling was likely induced by the outflow of cold pool outflow associated with alternation or propagation of convective systems embedded within the Mei-Yu front cloud system (Zhang et al., 2023). The resulting dense cold air wedging beneath the strong southwesterly LLJs can lift the jet axis above the cold-pool interface, further enhancing uplift and promoted rainfall (Luo et al., 2014). This in turn facilitated the final re-intensification of the jet structure (Fig. 7b and 8b). Importantly, this configuration sharply enhances low-level vertical wind shear and horizontal convergence (Fig. 12b), further promoting HR development. For LLJ_non-HR events, weaker thermodynamic support and diminished dynamic forcing with consistently lower LLJ indices within 60 min preceding rainfall resulted in insufficient lift to sustain HR. Compared with the disordered fluctuations of the LLJ_non-HR events, these results emphasized the importance of thermal-dynamic synergy influenced by LLJs evolution in triggering HR.

During Phase 3 in ROI-3, LLJ_HR events featured prominent thermal compensation (surface $\Delta\theta_e$ > 1K, 850hPa $\Delta\theta_e$> 2K versus non-HR events)—despite possessing generally weaker dynamical forcing compared to other phases (Fig. 12c). Temporally, the evolution was marked by distinct pulsations: The LLJ index exhibited a rapid rise (from ~0.03 to ~0.06) starting 84 min prior to HR onset (Fig. 12c) driven by a surge of LLJs profiles, while VWS peaked synchronously with the maximum LLJ frequency. Subsequently, a secondary peak in both the LLJ index and VWS was observed between –60 and –48 min. Although the subsequent declines in wind speed and frequency led to notable fluctuations in these parameters, the VWS and LLJ index underwent substantial intensification ((with VWS increasing by ~1.5 s^{-1}) in the final 24 min, driven by the rapid acceleration of the LLJ wind field. This co-evolution with rapid surface warming (increase of 0.25 K) released convective instability and enhanced convergence (Fig. 10). Nevertheless, the overall weaker dynamical conditions likely limited the depth and organization of convection, explaining the reduced probability of heavier rainfall compared to other phases. In contrast, during LLJ non-HR events, the LLJ index (~0.03) and θ_e vary rather gradually.

During Phase 4 in ROI-4, under the favorably thermal environments (θ_e > 346 K), LLJ_HR events showed a two-stage dynamic intensification. Initially, the LLJ index surged, while the VWS and jet intensity reached synchronous secondary peaks at –72 min. In the second stage, VWS increased rapidly by ~0.9 (Fig. 12d), and the LLJ index maintained an overall upward trend, peaking immediately prior to onset due to the surging jet. But LLJ_non-HR events showed weakening trends in both dynamic and thermodynamic conditions during the final 30 min and exhibited weaker changes (ΔVWS < 0.45 s^{-1}, ΔLLJ index < 0.02), reflecting an absence of the coordinated intensification necessary to initiate and sustain HR.

Although the evolution paths of the thermodynamic environment vary across different phases, a universal cross-region precursor emerges: the LLJ index and VWS consistently exhibits a strengthening or stabilizing trend in the final approximately 30 min preceding HR onset, operating in concert with significant low-level warming (rising θ_e). In contrast, non-HR events generally lack this culminating dynamical intensification. Overall, these results adequately showcase the sensitivity of regional HR to the fine-scale structural evolution of LLJs and their coupling with thermodynamic environments.

4. Summary and concluding remarks

Wind profile measurements from a nationwide network of 31 RWPs during the warm seasons (April–October) of 2023–2024 were utilized to characterize the minute-scale evolution of LLJs as dynamic precursors to nocturnal rainfall across China. By systematically comparing the vertically resolved behaviors of LLJs within the 2-hour window preceding nocturnal HR and non-HR events across four distinct rainy season phases, this study elucidates the critical dynamic-thermodynamic related to LLJs distinctions governing rainfall intensity.

Statistical analysis reveals that at the national scale, nocturnal rainfall accounted for nearly half of the total warm-season precipitation, with 56% of these nocturnal events exhibiting LLJ influence within the preceding 2 hours. In the key ROIs,

approximately 45.0% of identified HR events were associated with LLJs. Generally, these LLJ events exhibited a distinct probability advantage in producing heavier rainfall intensities compared to non-LLJ events, underscoring the strong linkage between LLJs and nocturnal HR.

Pronounced differences in LLJ evolution were consistently observed between HR and non-HR events across all phases, despite regional variations in synoptic forcing. During Phase 1 in ROI-1, a bimodal vertical distribution of LLJs and their rapid thermodynamic-dynamic co-intensification starting 84 min prior to rainfall were identified as key precursors of LLJ_HR events, in sharp contrast to the decoupled dynamics of LLJ_non-HR events. Phase 2 (ROI-2) was characterized by a distinct oscillatory process, where HR events featured a rapid descent of the LLJ core below 1 km followed by a robust rebound, distinguishing them from the quasi-steady state of LLJ_non-HR cases. In Phase 3 (ROI-3), LLJ_HR events exhibited significant thermal compensation and bimodal pulsations (peaks at –96 and –48 min), with a critical final-stage intensification serving as the decisive trigger. Similarly, Phase 4 (ROI-4) featured a distinctive two-stage intensification, where a rapid LLJ surge within 48 min of onset distinguished LLJ_HR events from the significantly attenuated dynamical structures of LLJ_non-HR events.

Although the specific dynamical pathways vary across different phases, all LLJ_HR events exhibit a “final-stage intensification” of the LLJs (LLJs strength, VWS and LLJ index) specifically within the 30 min preceding rainfall in synergy with thermodynamic instability (rising θ_e). This result can confirm the universality of the final-stage low-level dynamic intensification observed in our previous analysis (Li et al., 2024) as a robust trigger for nocturnal HR across diverse monsoon regions. Crucially, however, the current work identifies a novel “preparatory adjustment” phase (30–120 minutes prior) for LLJs structure (LLJs frequency, strength and height) that was not fully resolved in the regional study. This national-scale analysis reveals that the final dynamic trigger is contingent upon this earlier synergistic coupling of minute-scale jet evolution and thermodynamic destabilization. This coupled “rapid reorganization” process constitutes the essential, nationally valid precondition for HR

generation, contrasting with the quasi-steady evolution observed in LLJ_non-HR events. This underscores that the occurrence and intensity of nocturnal rainfall are ultimately regulated by regionally specific thermo-dynamic interactions modulated by the evolution of fine vertical structure of the LLJ.

This study establishes distinct dynamic-rainfall linkages associated with LLJs across different warm-season rainy periods in China. Future research should: (1) expand multi-source observations to establish dynamic thresholds for early forecasting systems of nocturnal rainfall, and (2) develop quantitative frameworks relating LLJ structural evolution to rainfall intensity, offering theoretical support for optimizing physical processes in LLJ parameterization schemes within high-resolution numerical models. Additionally, the physical mechanisms governing evolution of LLJs height or strength immediately preceding rainfall onset require further investigation.

Data Availability

The LLJs retrieved from the RWP network can be acquired from https://doi.org/10.5281/zenodo.17176759 (Li and Guo, 2025). The data from the weather station are obtained from the China Meteorological Data Service Centre at https://data.cma.cn/en, and the original ERA5 reanalysis data used here are available from the ECMWF in Hersbach et al. (2020).

Acknowledgments

This work was supported by the National Natural Science Foundation of China under Grants of 42325501, the Science and Technology Supporting Project of Guizhou Province ([2023]236) and by the National Key Research and Development Program of China under grant 2024YFC3013001. Last but not least, we appreciated tremendously the constructive comments and suggestions made by the anonymous reviewers that significantly improved the quality of our manuscript.

Author Contributions

The study was completed with close cooperation between all authors. JG designed the research framework; NL performed the analysis and drafted the original manuscript

with contribution from JG; JG, XG, ZZ, YZ. JG, NT, YW, and YZ helped revise the manuscript.

Completing interests

The authors declare that they have no conflict of interest.

References

Anthes, R. A., Kuo, Y. H., Benjamin, S. G., and Li, Y. F: The evolution of the mesoscale environment of severe local storms: Preliminary modeling results, Mon. Weather Rev., 110(9), 1187-1213, doi:10.1175/1520-0493(1982)110,1187: TEOTME.2.0.CO;2, 1982.

Bai, L., Chen, G., Huang, Y., and Meng, Z.: Convection initiation at a coastal rainfall hotspot in South China: Synoptic patterns and orographic effects, J. Geophys. Res. Atmos., 126(24), e2021JD034642, doi: 10.1029/2021JD034642, 2021.

Blackadar, A. K.: Boundary layer wind maxima and their significance for the growth of nocturnal inversions, Bull. Am. Meteorol. Soc., 38(5), 283-290, doi:10.1175/1520-0477-38.5.283, 1957.

Bonner, W. D.: Climatology of the low-level jet, Mon. Weather Rev., 96(12), 833-850. doi:10.1175/1520-0493(1968) 096<0833:COTLLJ>2.0.CO;2, 1968.

Cao, Q., J. Guo, C. Xue, Z. Li, H. Xu, N. Li, Y. Sun, Z. Zhang, Y. Wang, J. Chen, Y. Zhou, and T. Chen: Divergent Sounding-derived Precursor Pathways Enable Discrimination of Dry versus Wet Severe Convective Winds. Geophysical Research Letters, 52, e2025GL117491. https://doi.org/10.1029/2025GL117491, 2025.

Carbone, R. E., and Tuttle, J. D.: Rainfall occurrence in the US warm season: The diurnal cycle, J. Clim., 21(16), 4132-4146, doi:10.1175/2008JCLI2275.1, 2008.

Chen, G., Sha, W., Iwasaki, T., and Wen, Z.: Diurnal Cycle of a Heavy Rainfall Corridor over East Asia, Mon. Weather Rev., 145(8), 3365-3389, doi:10.1175/mwr-d-16-0423.1, 2017.

Chen, H., Zhou, T., Neale, R. B., Wu, X., and Zhang, G. J.: Performance of the new NCAR CAM3. 5 in East Asian summer monsoon simulations: Sensitivity to modifications of the convection scheme, J. Clim., 23(13), 3657-3675, doi:10.1175/2010JCLI3022.1, 2010.

Chen, T., Guo, J., Guo, X., Zhang, Y., Xu, H., and Zhang, D.-L.: On the multiscale processes leading to an extreme gust wind event in East China: Insights from radar

649 wind profiler mesonet observations. Journal of Geophysical Research:
650 Atmosphere, 129, e2024JD041484, doi: 10.1029/2024JD041484, 2024.
651 Chen, X., F. Zhang, and K. Zhao: Diurnal Variations of the Land-Sea Breeze and Its
652 Related Precipitation over South China. J. Atmos. Sci., 73, 4793–4815,
653 doi:10.1175/JAS-D-16-0106.1, 2016.
654 Chen, Y. L., and Li, J.: Large-scale conditions favorable for the development of heavy
655 rainfall during TAMEX IOP 3, Mon. Weather Rev., 123(10), 2978-3002, 1995.
656 China Meteorological Administration: Specification for Automatic Observation of
657 Ground Meteorology. China Meteorological Press, 2020.
658 Davis, C. A., Maning, W. K., Carbone, R., Trier, S., and Tuttle, J.: Coherence of warm-
659 season continental rainfall in numerical weather prediction models, Mon. Weather
660 Rev., 131, 2667-2679, doi:10.1175/1520-
661 0493(2003)131<2667:COWCRI>2.0.CO;2, 2003.
662 Dong, F., Zhi, X., Zhang, L., and Ye, C.: Diurnal variations of coastal boundary layer
663 jets over the northern South China Sea and their impacts on diurnal cycle of
664 rainfall over southern China during the early-summer rainy season, Mon. Weather
665 Rev., 149(10), 3341-3363, doi:10.1175/MWR-D-20-0292.1, 2021.
666 Doubler, D. L., Winkler, J. A., Bian, X., Walters, C. K., and Zhong, S.: An NARR-
667 derived climatology of southerly and northerly low-level jets over North America
668 and coastal environs, J. Appl. Meteorol. Climatol., 54(7), 1596-1619,
669 doi:10.1175/JAMC-D-14-0311.1, 2015.
670 Du, Y., and Chen, G.: Heavy Rainfall Associated with Double Low-Level Jets over
671 Southern China. Part II: Convection Initiation, Mon. Weather Rev., 147(2), 543-
672 565, doi:10.1175/mwr-d-18-0102.1, 2019.
673 Du, Y., and G. Chen: Heavy Rainfall Associated with Double Low-Level Jets over
674 Southern China. Part I: Ensemble-Based Analysis, Monthly Weather Review, 146,
675 3827–3844, doi: 10.1175/MWR-D-18-0101.1, 2018.
676 Du, Y., Chen, G., Han, B., Bai, L., and Li, M.: Convection initiation and growth at the
677 coast of South China. Part II: Effects of the terrain, coastline, and cold pools, Mon.
678 Weather Rev., 148(9), 3871-3892, doi:10.1175/MWR-D-20-0090.1, 2020.

679 Du, Y., Zhang, Q., Ying, Y., and Yang, Y.: (2012). Characteristics of low-level jets in
680 Shanghai during the 2008-2009 warm seasons as inferred from wind profiler radar
681 data, J. Meteorol. Soc. Jpn. Ser. II, 90(6), 891-903, doi:10.2151/jmsj.2012-603,
682 2012.
683 Fu, S. M., Jin, S. L., Shen, W., Li, D. Y., Liu, B., & Sun, J. H.: A kinetic energy budget
684 on the severe wind production that causes a serious state grid failure in Southern
685 Xinjiang China, Atmospheric Science Letters, 21(7), e977, 2020.
686 Gebauer, J. G., Shapiro, A., Fedorovich, E., and Klein, P.: (2018). Convection Initiation
687 Caused by Heterogeneous Low-Level Jets over the Great Plains, Mon. Weather
688 Rev., 146(8), 2615-2637, doi:10.1175/mwr-d-18-0002.1, 2018.
689 Guo, J., Liu, B., Gong, W., Shi, L., Zhang, Y., Ma, Y., Zhang, J., Chen, T., Bai, K.,
690 Stoffelen, A., de Leeuw, G., and Xu, X.: Technical note: First comparison of wind
691 observations from ESA's satellite mission Aeolus and ground-based radar wind
692 profiler network of China, Atmos. Chem. Phys., 21, 2945-2958, doi: 10.5194/acp-
693 21-2945-2021, 2021 (data available at: https://data.cma.cn, last access: 11 January
694 2024).
695 Guo, X., Guo, J., Chen, T., Li, N., Zhang, F., and Sun, Y.: Revisiting the evolution of
696 downhill thunderstorms over Beijing: a new perspective from a radar wind profiler
697 mesonet, Atmos. Chem. Phys., 24(14), 8067-8083, doi:10.5194/acp-24-8067-
698 2024, 2024.
699 Guo, X., Guo, J., Zhang, D. L., and Yun, Y.: Vertical divergence profiles as detected
700 by two wind-profiler mesonets over East China: Implications for nowcasting
701 convective storms, Q. J. R. Meteorol. Soc., 149(754), 1629-1649.
702 doi:10.1002/qj.4474, 2023.
703 Hersbach, H., Bell, B., Berrisford, P., Biavati, G., Horányi, A., Muñoz Sabater, J.,
704 Nicolas, J., Peubey, C., Radu, R., Rozum, I., Schepers, D., Simmons, A., Soci, C.,
705 Dee, D.and Thépaut, J-N.: ERA5 hourly data on pressure levels from 1940 to
706 present. Copernicus Climate Change Service (C3S) Climate Data Store (CDS),
707 doi: 10.24381/cds.bd0915c6 (Accessed on 06-05-2024), 2023.

Higgins, R. W., Yao, Y., Yarosh, E. S., Janowiak, J. E., and Mo, K. C.: Influence of the Great Plains low-level jet on summertime precipitation and moisture transport over the central United States, J. Clim., 10(3), 481-507, 1997.

Hodges, D., and Pu, Z.: Characteristics and Variations of Low-Level Jets and Environmental Factors Associated with Summer Precipitation Extremes over the Great Plains. J. Clim., 32(16), 5123-5144, doi:10.1175/JCLI-D-18-0553.1, 2019.

Holton, J. R.: The diurnal boundary layer wind oscillation above sloping terrain, Tellus, 19(2), 200-205, doi: 10.3402/tellusa.v19i2.9766, 1967.

Horinouchi, T., Matsumura, S., Ose, T., and Takayabu, Y. N.: Jet-precipitation relation and future change of the mei-yu-baiu rainband and subtropical jet in CMIP5 coupled GCM simulations, J. Clim., 32(8), 2247-2259, doi:10.1175/JCLI-D-18-0426.1, 2019.

Huang, X., Sun, J., and Liu, W.: The interaction between low-level jet evolution and severe convective rainstorms under topographic effect, Acta Meteorol. Sin., 78(4), 551-567, 2020.

Li, N., and Guo, J.: Data for wind profiles associated with LLJs obtained from RWP observations during the warm season (April-October) of 2023-2024 in China [Data set]. Zenodo. https://doi.org/10.5281/zenodo.17176759, 2025.

Li, N., Guo, J., Wu, M., Zhang, F., Guo, X., Sun, Y., Zhang Z., Liang L., Chen T.: Low-level jet and its effect on the onset of summertime nocturnal rainfall in Beijing, Geophys. Res. Lett., 51, e2024GL110840, doi:10.1029/2024GL11084, 2024.

Li, X., and Du, Y.: Statistical relationships between two types of heavy rainfall and low-level jets in South China, J. Clim., 34(21), 8549-8566, doi:10.1175/JCLI-D-21-0121.1, 2021.

Liu, B., Ma, Y., Guo, J. and Wei, G.: Boundary layer heights as derived from ground-based radar wind profiler in Beijing, IEEE Trans. Geosci. Remote Sens., 57, 8095-8104, doi:10.1109/TGRS.2019.2918301, 2019.

Liu, X., Luo, Y., Huang, L., Zhang, D. L., & Guan, Z: Roles of double low-level jets in the generation of coexisting inland and coastal heavy rainfall over south China

737 during the presummer rainy season, Journal of Geophysical Research:
738 Atmospheres, 125(18), e2020JD032890, 2020.
739 Luo, Y., Gong, Y., and Zhang, D. L.: Initiation and organizational modes of an extreme-
740 rain-producing mesoscale convective system along a mei-yu front in East China,
741 Mon. Weather Rev., 142(1), 203-221, doi:10.1175/MWR-D-13-00111.1, 2014.
742 Maddox, R. A.: Large-scale meteorological conditions associated with midlatitude,
743 mesoscale convective complexes, Mon. Weather Rev., 111(7), 1475-1493, 1983.
744 Marengo, J. A., Soares, W. R., Saulo, C., and Nicolini, M.: Climatology of the low-
745 level jet east of the Andes as derived from the NCEP-NCAR reanalyses:
746 Characteristics and temporal variability, J. Clim., 17(12), 2261-2280, 2004.
747 Markowski, P., & Richardson, Y.: Mesoscale meteorology in midlatitudes, John Wiley
748 & Sons, 2011.
749 Miao, Y., Guo, J., Liu, S., Wei, W., Zhang, G., Lin, Y., and Zhai, P.: The Climatology
750 of Low-Level Jet in Beijing and Guangzhou, China, J. Geophys. Res. Atmos.,
751 123(5), 2816-2830. doi:10.1002/2017jd027321, 2018.
752 Mitchell, M. J., Arritt, R. W., and Labas, K.: A climatology of the warm season Great
753 Plains low-level jet using wind profiler observations, Weather Forecast., 10(3),
754 576-591, 1995.
755 Molod, A., Salmun, H. and Collow, A.B.M.: Annual cycle of planetary boundary layer
756 heights estimated from wind profiler network data, J. Geophys. Res. Atmos., 124,
757 6207-6221, doi:10.1029/2018JD030102, 2019.
758 Monaghan, A. J., Rife, D. L., Pinto, J. O., Davis, C. A., and Hannan, J. R.: Global
759 precipitation extremes associated with diurnally varying low-level jets, J. Clim.,
760 23(19), 5065-5084, 2010.
761 Pan, H., and Chen, G.: Diurnal variations of precipitation over North China regulated
762 by the mountain-plains solenoid and boundary-layer inertial oscillation, Adv.
763 Atmos. Sci., 36(8), 863-884, doi:10.1175/2010JCLI3515.1, 2019.
764 Pitchford, K. L., and London, J.: The low-level jet as related to nocturnal thunderstorms
765 over Midwest United States, J. Appl. Meteorol., 1(1), 43-47, 1962.

766 Rasmussen, K. L., and Houze Jr, R. A.: Convective initiation near the Andes in
767 subtropical South America, Mon. Weather Rev., 144(6), 2351-2374,
768 doi:10.1175/MWR-D-15-0058.1, 2016.
769 Reif, D. Q., and Bluestein, H.: A 20-year climatology of nocturnal convection initiation
770 over the central and southern great plains during the warm season, Mon. Weather
771 Rev., 145, 1615-1639, doi:10.1175/MWR-D-16-0340.1, 2017.
772 Roots, M., Sullivan, J. T., and Demoz, B.: Mid-Atlantic nocturnal low-level jet
773 characteristics: a machine learning analysis of radar wind profiles, Atmos. Meas.
774 Tech., 18(5), 1269-1282, doi:10.5194/amt-18-1269-2025, 2025.
775 Stensrud, D. J.: Importance of low-level jets to climate: A review, J. Clim., 1698-1711,
776 1996.
777 Subrahmayam, K. V., Udupa, S. R., Kumar, K. K., Ramana, M. V., Srinivasulu, J., and
778 Bothale, R. V.: Prediction of zonal wind using machine learning algorithms:
779 Implications to future projections of Indian monsoon jets, J. Indian Soc. Remote
780 Sens., 52(2), 371-381, 2024.
781 Sun, S. Q., Zhai, G. H., and Lorenzo, D. O.: The relationship between large-scale low-
782 level jet over east asia and monsoon as well as cross-equatorial currents in
783 summer, Acta Meteorol. Sin., 1(1), 43-50, 1986.
784 Trier, J. W. Wilson, D. A. Ahijevych, and R. A. Sobash : Mesoscale vertical motions
785 near nocturnal convection initiation in PECAN, Mon. Weather Rev., 145, 2919-
786 2941, doi:10.1175/MWR-D-17-0005.1, 2017.
787 Trier, S. B., Davis, C. A., Ahijevych, D. A., Weisman, M. L., and Bryan, G. H.:
788 Mechanisms supporting long-lived episodes of propagating nocturnal convection
789 within a 7-day WRF model simulation, J. Atmos. Sci., 63(10), 2437-2461, doi:
790 10.1175/JAS3768.1, 2006.
791 Tuttle, J. D., and Davis, C. A.: Corridors of warm season precipitation in the central
792 United States. Mon. Weather Rev., 134(9), 2297-2317, doi:10.1175/MWR3188.1,
793 2006.
794 Uccellini, L. W., and D. R. Johnson: The coupling of upper and lower tropospheric jet
795 streaks and implications for the development of severe convective storms.

796 Monthly Weather Review, 107, 682-703, doi: 10.1175/1520-
797 0493(1979)107,0682:TCOUAL.2.0.CO;2, 1979.
798 Walters, C. K., Winkler, J. A., Shadbolt, R. P., van Ravensway, J., and Bierly, G. D.:
799 A long-term climatology of southerly and northerly low-level jets for the central
800 United States, Ann. Assoc. Am. Geogr., 98(3), 521-552, 2008.
801 Wang, D., Zhang, Y., and Huang, A.: Climatic features of the south-westerly low-level
802 jet over southeast China and its association with precipitation over east China,
803 Asia-Pac. J. Atmos. Sci., 49(3), 259-270, doi:10.1007/s13143-013-0025-y, 2013.
804 Wang, W. C., Gong, W., and Wei, H.: A regional model simulation of the 1991 severe
805 precipitation event over the Yangtze-Huai River valley. Part I: Precipitation and
806 circulation statistics, J. Clim., 13(1), 74-92, doi:10.1175/1520-
807 0442(2000)013<0074:ARMSOT>2.0.CO;2, 2000.
808 Weckwerth, T. M., and Wakimoto, R. M.: The initiation and organization of convective
809 cells atop a cold-air outflow boundary, Mon. Weather Rev., 120(10), 2169–2187,
810 doi:10.1175/ 1520-0493(1992)120,2169:TIAOOC.2.0.CO;2, 1992.
811 Weckwerth, T. M., Hanesiak, J., Wilson, J. W., et al.: Nocturnal convection initiation
812 during PECAN 2015, Bull. Am. Meteorol. Soc., 100(11), 2223-2239,
813 doi::10.1175/BAMS-D-18-0299.1, 2019.
814 Wei, W., Zhang, H. S., and Ye, X. X.: Comparison of low-level jets along the north
815 coast of China in summer, J. Geophys. Res. Atmos., 119(16), 9692-9706.
816 doi:10.1002/2014jd021476, 2014.
817 Weisman, M. L., Trapp, R. J., Romine, G. S., Davis, C., Torn, R., Baldwin, M., Bosart,
818 L., Brown, J., Coniglio, M., Dowell, D., Evans, A. C., Galarneau, T. J., Haggerty,
819 J., Hock, T., Manning, K., Roebber, P., Romashkin, P., Schumacher, R., Schwartz,
820 C. S., Sobash, R., Stensrud, D., and Trier, S. B.: The mesoscale predictability
821 experiment (MPEX), Bull. Am. Meteorol. Soc., 96(12), 2127-2149,
822 doi:10.1175/bams-d-13-00281.1, 2015.
823 Whiteman, C. D., Bian, X., and Zhong, S.: Low-level jet climatology from enhanced
824 Rawinsonde observations at a site in the southern Great Plains, J. Appl. Meteorol.,

825 36(10), 1363-1376, doi:10.1175/1520-
826 0450(1997)036%3C1363:LLJCFE%3E2.0. CO;2, 1997.
827 Xia, R., and Zhao, S.: Diagnosis and modeling of meso-scale systems of heavy rainfall
828 in warm sector ahead of front in South China (middle part of Guangdong province)
829 in June 2005, Chin. J. Atmos. Sci., 33(3), 2009.
830 Xue, M., Luo, X., Zhu, K., Sun, Z., and Fei, J.: The controlling role of boundary layer
831 inertial oscillations in Meiyu frontal precipitation and its diurnal cycles over
832 China, J. Geophys. Res. Atmos., 123(10), 5090-5115,
833 doi:10.1029/2018JD028368, 2018.
834 Yan, Y., Cai, X., Wang, X., Miao, Y., and Song, Y.: Low-level jet climatology of China
835 derived from long-term radiosonde observations, J. Geophys. Res. Atmos.,
836 126(20), e2021JD035323, doi:10.1029/2021JD035323, 2021.
837 Yu, R., Li, J., Chen, H., and Yuan, W.: Progress in studies of the precipitation diurnal
838 variation over contiguous China, J. Meteorol. Res., 28(5), 877-902,
839 doi:10.1007/s13351-014-3272-7, 2014.
840 Zamora, R.J., Shapiro, M.A. and Doswell, C.A., III.: The diagnosis of upper
841 tropospheric divergence and ageostrophic wind using profiler wind observations,
842 Mon. Weather Rev., 115, 871-884, doi:10.1175/1520-0493(1987)1152.0.CO;2,
843 1987.
844 Zhang, F., Zhang, Q., Sun, J., and Xu, J.: Convection initiation during the Meiyu
845 environment in the Yangtze-Huai River basin of China, J. Geophys. Res. Atmos.,
846 128(9), e2022JD038077, doi:10.1029/2022JD038077, 2023.
847 Zhang, M., and Meng, Z.: Warm-sector heavy rainfall in southern China and its WRF
848 simulation evaluation: A low-level-jet perspective, Mon. Weather Rev., 147(12),
849 4461-4480, doi:10.1175/MWR-D-19-0110.1, 2019.
850 Zhang, Y., Xue, M., Zhu, K., and Zhou, B.: What is the main cause of diurnal variation
851 and nocturnal peak of summer precipitation in Sichuan Basin, China? the key role
852 of boundary layer low-level jet inertial oscillations, J. Geophys. Res. Atmos.,
853 124(5), 2643-2664, doi:10.1029/2018jd029834, 2019.

Zhao, Y., Liao, J., Zhang, Q., Chen, J., Gong, X., Shi, Y., Shi, M., Yang, D., Fan, S., Zhou, X., Cao, L., and Hu, K.: Development of China Ground Climate Normal Value Dataset from 1991 to 2020, Chinese Journal of Atmospheric Sciences (in Chinese), 48(2), 555–571, doi:10.3878/j.issn.1006-9895.2204.22010, 2024.

860 Table 1. Table of Representative Radar Wind Profiler Stations in Mainland China

Region	Station		Longitude (°)	Latitude (°)	Altitude (m)
ROI-1	58839	MQ	118.86	26.22	160.70
	59046	LZ	109.46	24.36	314.40
	59137	JJ	118.54	24.81	124.80
	59287	GZ	113.48	23.21	65.00
	59758	HK	110.25	19.99	69.00
ROI-2	57461	YC	111.36	30.74	253.80
	57687	CS	112.79	28.11	119.00
	57793	YCN	114.36	27.79	132.00
	58238	BJ	118.90	31.93	40.60
	58321	HF	117.03	31.57	50.00
	58367	LH	121.47	31.18	5.00
	58459	XS	120.29	30.18	48.80
ROI-3	53463	HHHT	111.68	40.82	1152.10
	53772	TY	112.58	37.62	785.00
	54511	BJ	116.47	39.81	31.50
	54534	TS	118.10	39.65	23.20
	54602	BD	115.48	38.73	16.80
ROI-4	57816	GY	106.73	26.59	1197.60
	56290	XD	104.18	30.77	514.00
	56651	LJ	100.22	26.85	2382.40
Other stations	50936	BC	122.47	45.36	156.00
	51463	WLMQ	87.65	43.79	935.00
	51628	AKS	80.38	41.12	1107.10
	52754	GC	100.08	37.2	3301.50
	52889	LZ	103.89	36.06	1519.20
	57516	CQ	106.46	29.57	260.00
	53845	YA	109.45	36.58	1180.40
	54342	SY	123.51	41.73	50.00
	54857	QD	120.13	36.23	12.00
	55664	DR	87.07	28.63	4302.00
	57171	PDS	113.12	33.77	142.00

Figures

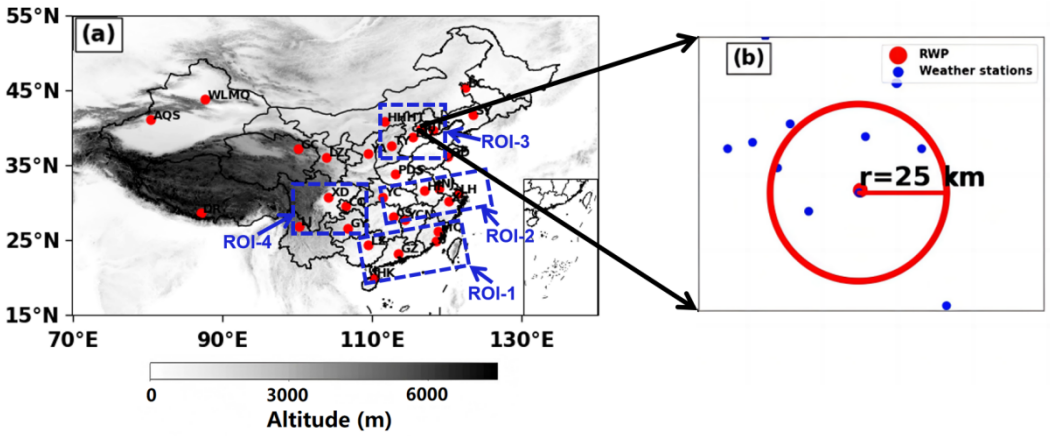

Figure.1 (a) Spatial distribution of 31 Radar Wind Profiler (RWP) stations across China, with four regions of interest (ROIs) demarcated by blue dashed boxes: ROI-1, ROI-2, ROI-3, and ROI-4. (b) Schematic of spatial co-location: Beijing Observatory's RWP (red circle) and rain gauges (black dots) within a 25-km radius

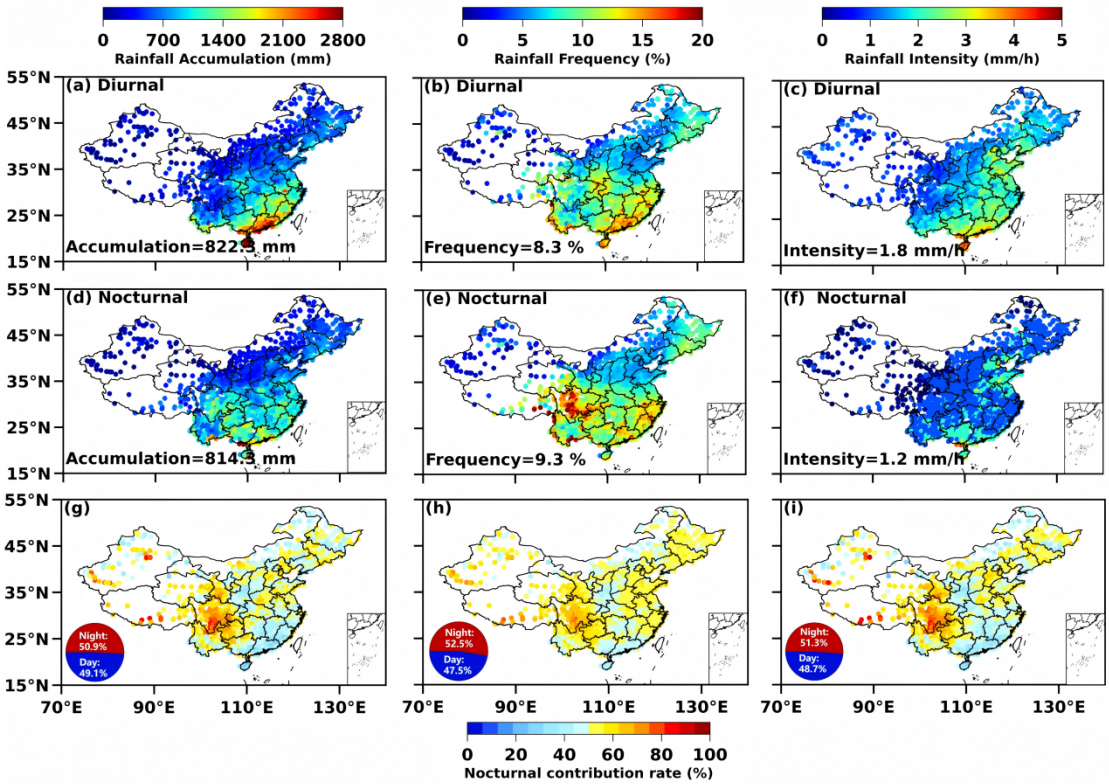

Figure 2. (a–c) Spatial distributions of accumulated rainfall (mm), rainfall frequency (%) and rainfall intensity (mm/h) in the daytime from April to October in 2023–2024. The numbers in the upper left corner represent the national average; (d–f) the same as (a–c), but in the nighttime; (g–i) Nocturnal contribution ratios of accumulated rainfall, frequency, and occurrence frequency of heavy rainfall (>75th percentile intensity). The pie charts illustrate the relative contribution rates of daytime (blue) and nighttime (red) at the national scale

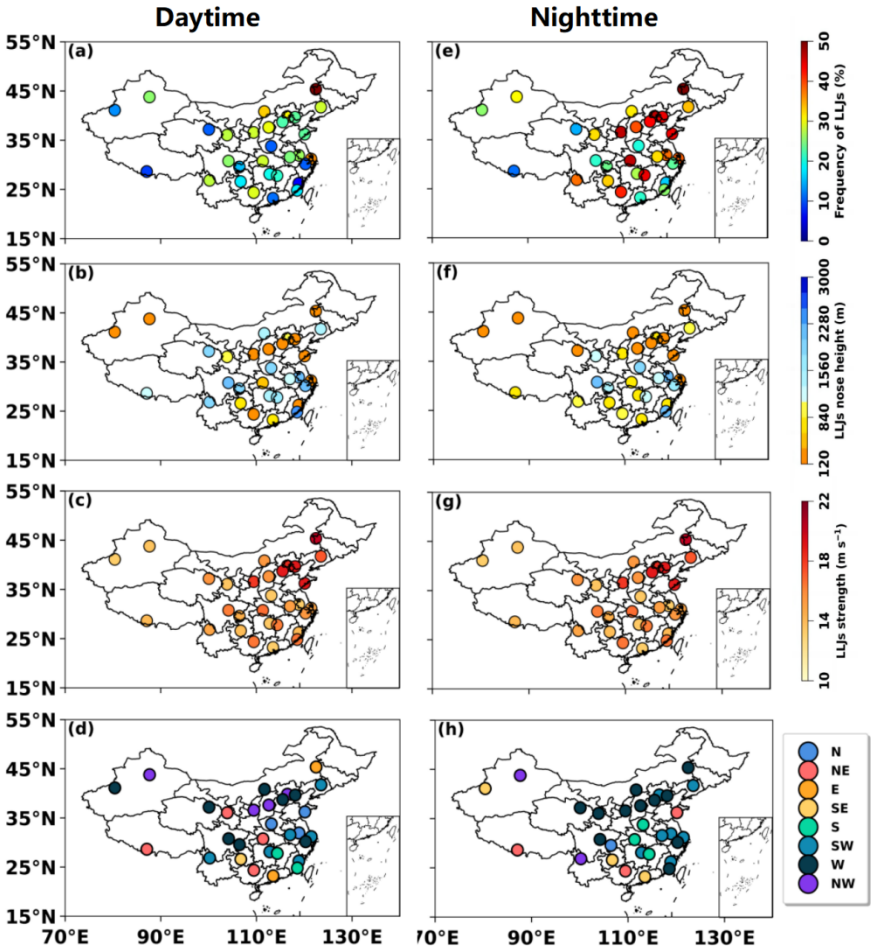

892

893 Figure 3. (a–d) Spatial distribution of occurrence frequency, height, strength, and the
894 dominant wind direction of LLJs observed by 31 RWP stations during April–October
895 from 2023 to 2024 in the daytime. (e–h) Same as (a–d), but in the nighttime.

896

897

898

899

900

901

902

903

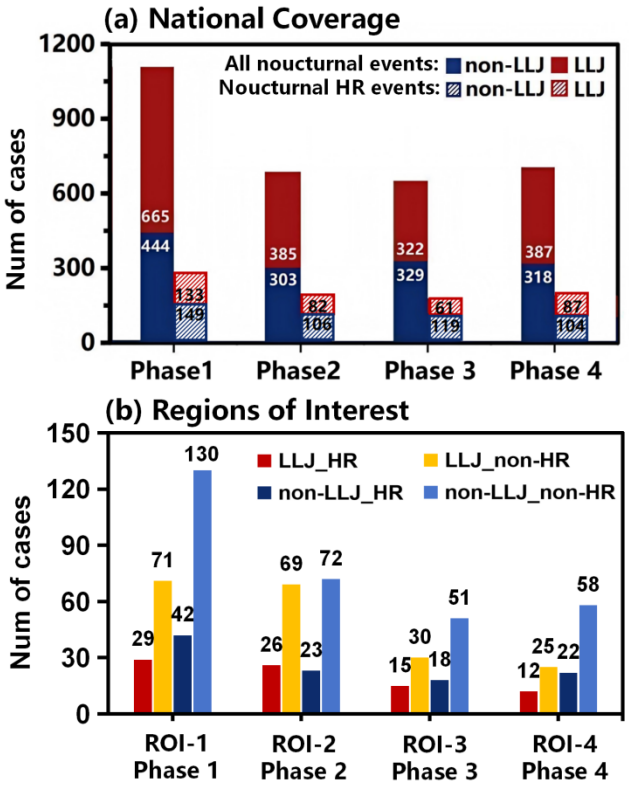

904

905 Figure 4. Statistics of all nocturnal rainfall events (solid-filled bars) and heavy rainfall
906 (HR; diagonally striped bars) events across China during four phases, categorized into
907 LLJ events (red) and non-LLJ events (blue). (b) Statistics of all nocturnal events within
908 the four ROIs (ROI-1 to ROI-4) during their corresponding phases, categorized into
909 four types: LLJ_HR (red), LLJ_non-HR (yellow), non-LLJ_HR (dark blue), and non-
910 LLJ_non-HR (light blue) events.

911

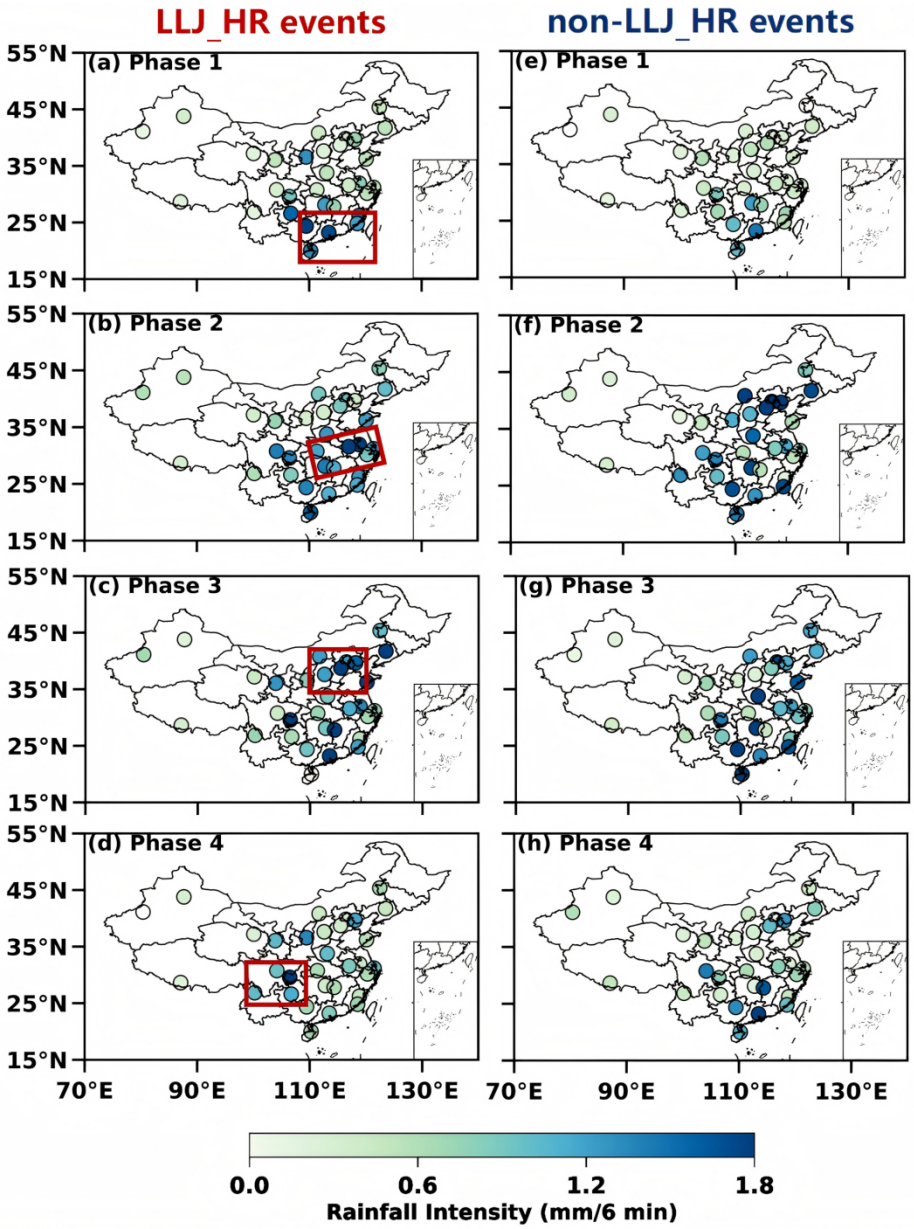

912

913 Figure 5. (a–d) Spatial distributions of average rain rate (mm/6 min) for nocturnal
914 LLJ_HR events during the warm season from Phase 1 to Phase 4 across China; (e–h)
915 Same as (a–d), but for non-LLJ_HR events. The red frame indicates four ROIs.

916

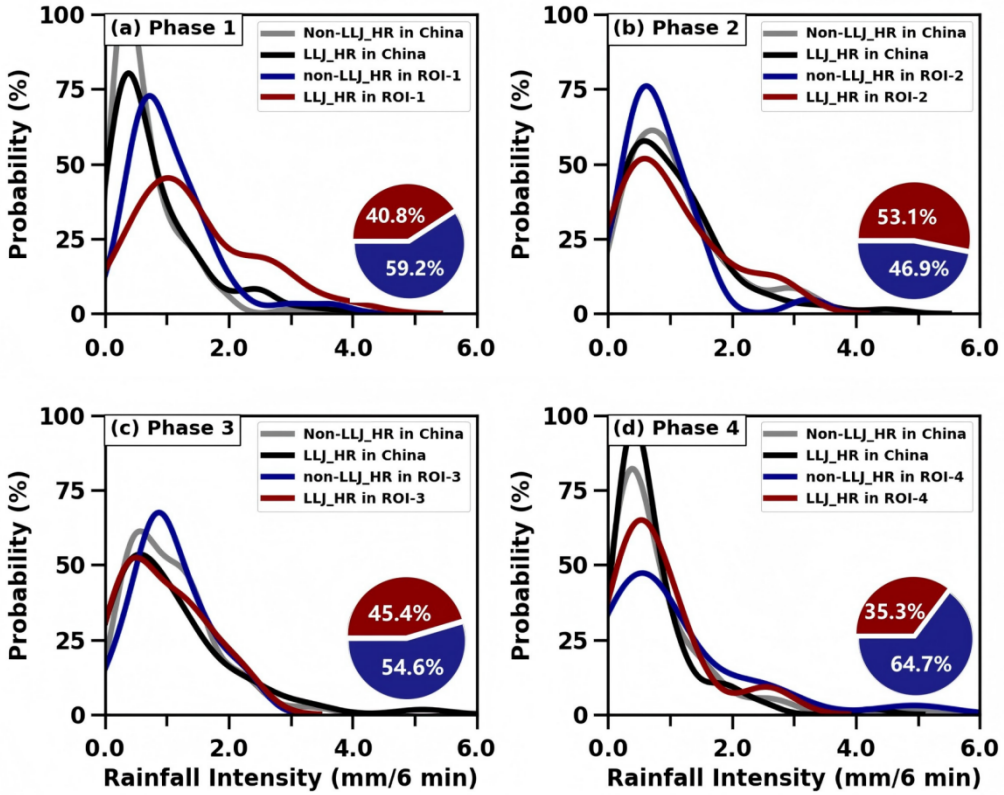

917

918 Figure 6. (a) Probability density distributions of average rain rate (mm/6 min) for
919 LLJ_HR events (black solid lines) and non-LLJ_HR events (gray solid lines) across
920 China during Phase 1, and specifically in ROI-1 for LLJ_HR events (red solid lines)
921 and non-LLJ_HR events (blue solid lines). (b-d) the same as panel (a), but for
922 comparisons between national-scale and other regional-scale events in ROI-2 during
923 Phase 2, ROI-3 during Phase 3, and ROI-4 during Phase 4. The pie chart at the lower
924 right shows the proportion distribution of LLJ_HR (red) and non-LLJ_HR (blue) events
925 in these key regions during each period

926

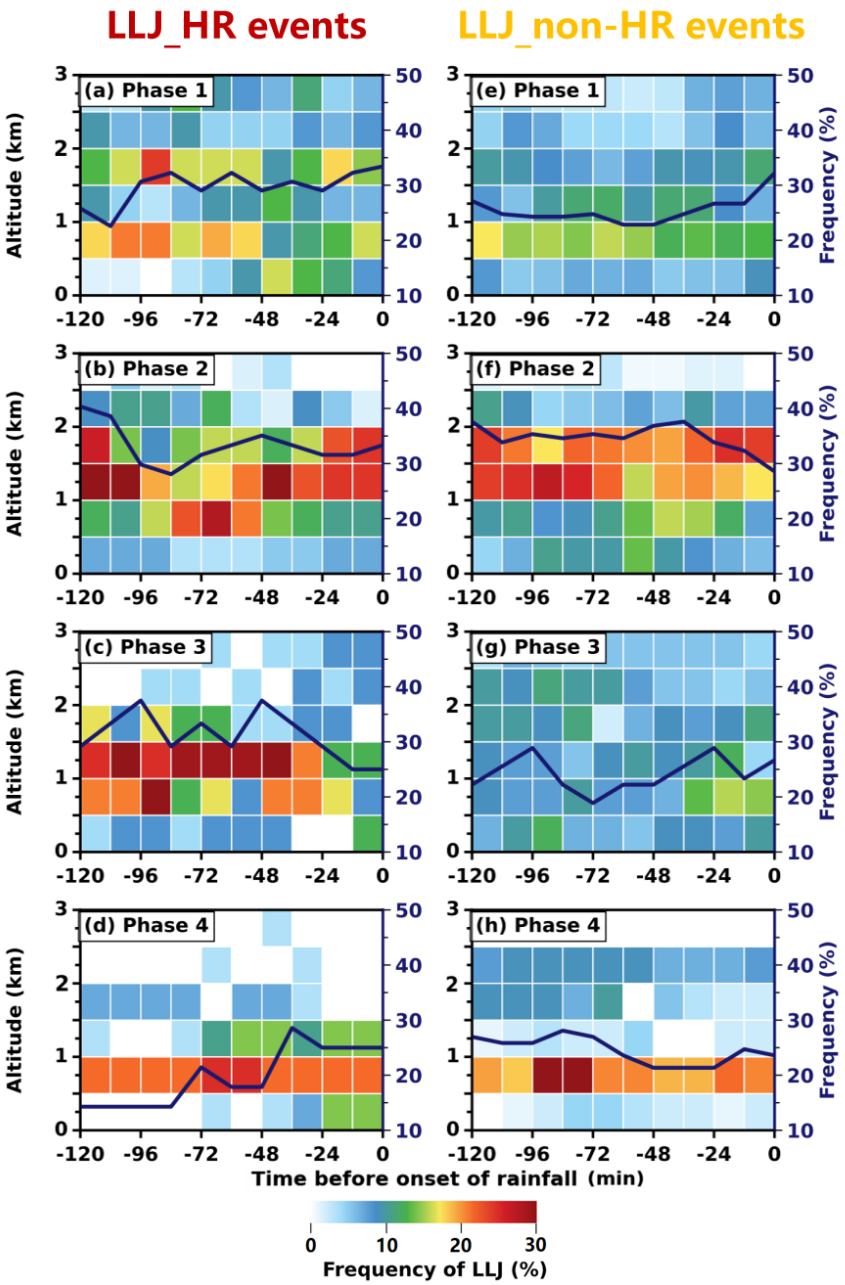

927

928 Figure 7. Time-height evolution of LLJ occurrence frequency (color shading, every 12
929 min, within 500 m vertical bins) detected by RWP with 2 hours preceding nocturnal
930 rainfall in LLJ_HR events in (a) ROI-1 during Phase 1, (b) ROI-2 during Phase 2, (c)
931 ROI-3 during Phase 3, and (d) in ROI-4 during Phase 4. Dark blue solid lines denote
932 accumulated LLJ frequency over 0–3 km latitude. (e-h) Same as (a-d), but for LLJ_non-
933 HR events

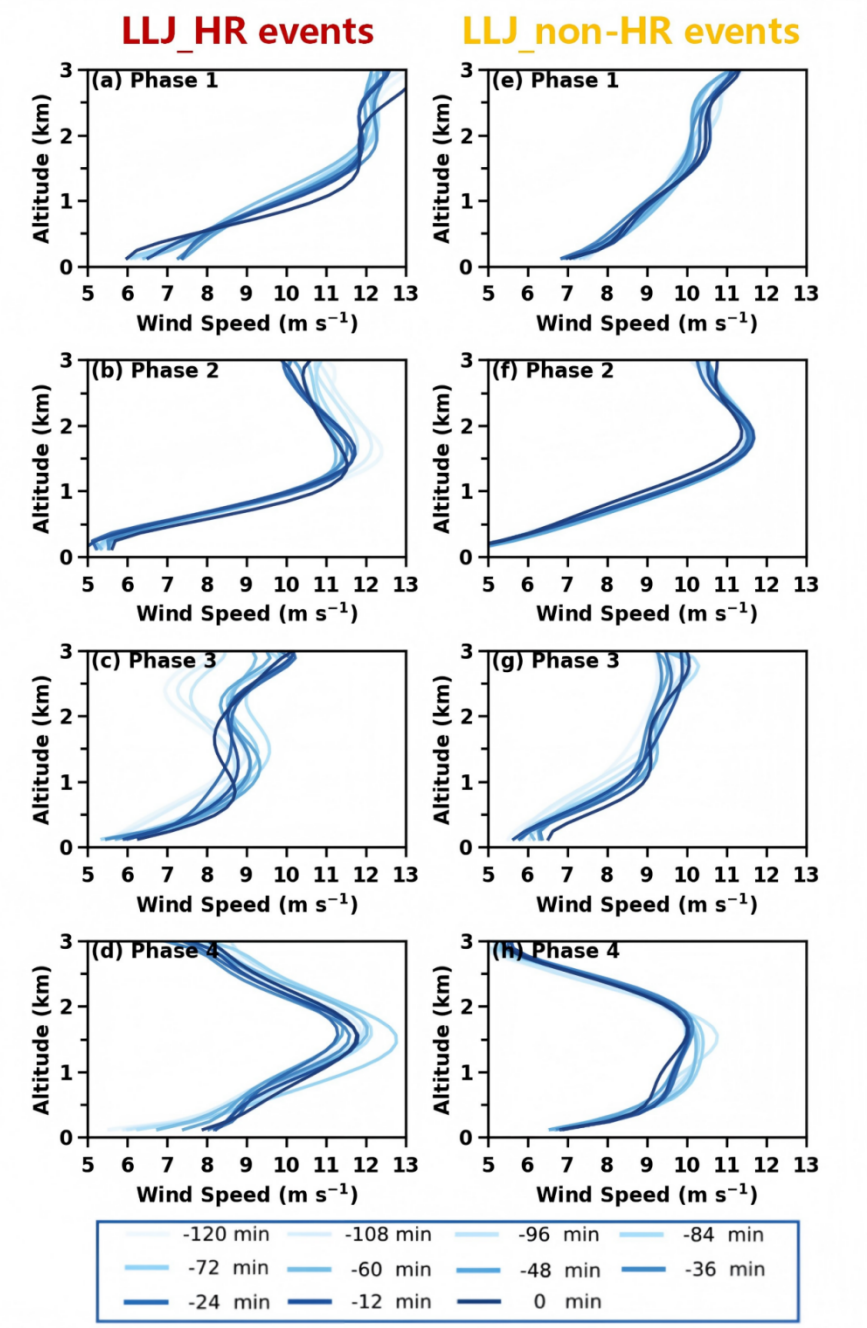

934

935 Figure 8. (a-d) Evolution of RWP-detected mean wind profiles of LLJs (blue solid lines,
936 every 12 min) within 2 hours preceding nocturnal rainfall in LLJ_HR events in (a) ROI-
937 1 during Phase 1, (b) ROI-2 during Phase 2, (c) ROI-3 during Phase 3, and (d) in ROI-
938 4 during Phase 4. (e-h) Same as (a-d), but for LLJ_non-HR events

939

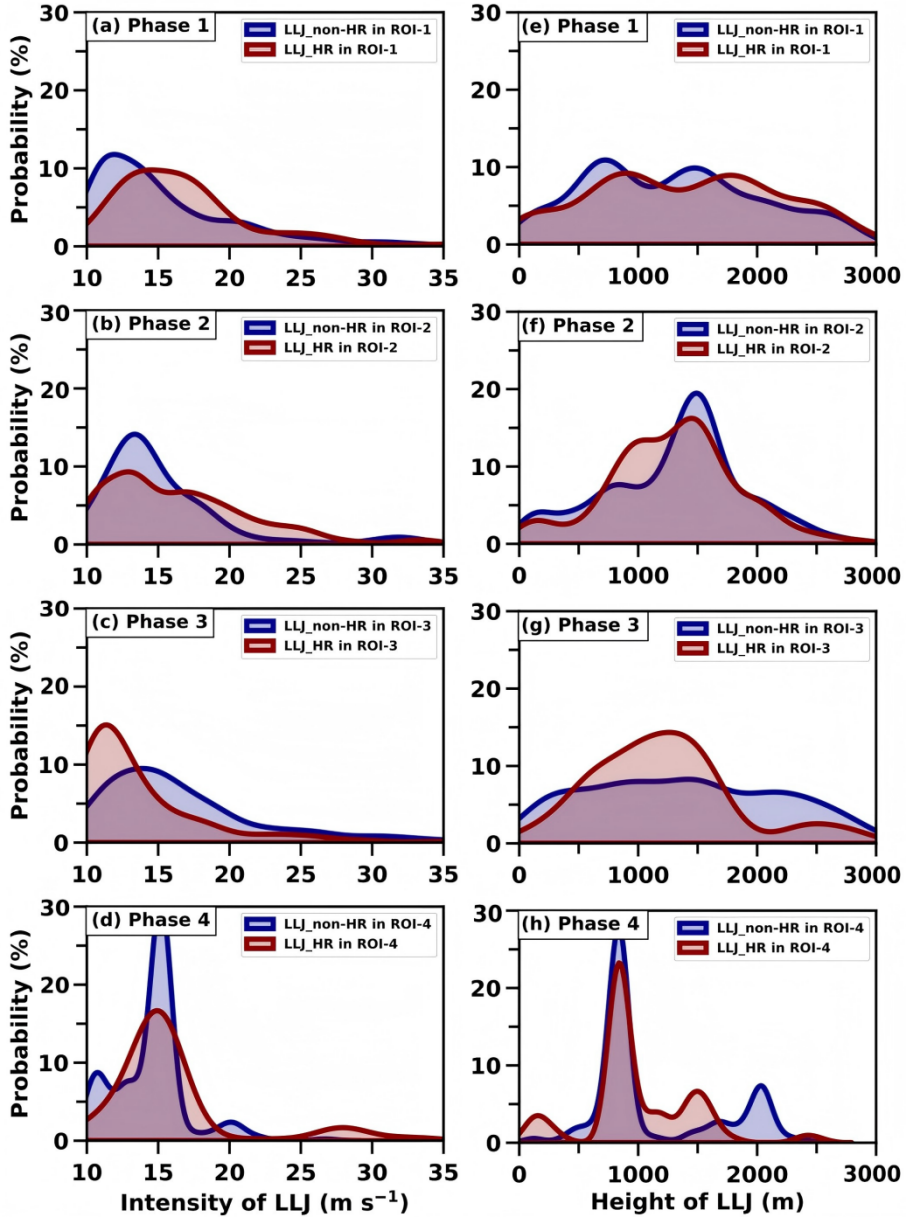

940

941

942 Figure 9. Probability density distributions of jet core intensity from RWP observations
943 within 2 hours preceding nocturnal rainfall in LLJ_HR events in (a) ROI-1 during Phase
944 1, (b) ROI-2 during Phase 2, (c) ROI-3 during Phase 3, and (d) in ROI-4 during Phase
945 4. (e-h) Same as (a-d), but for the height of LLJs

946

947

948

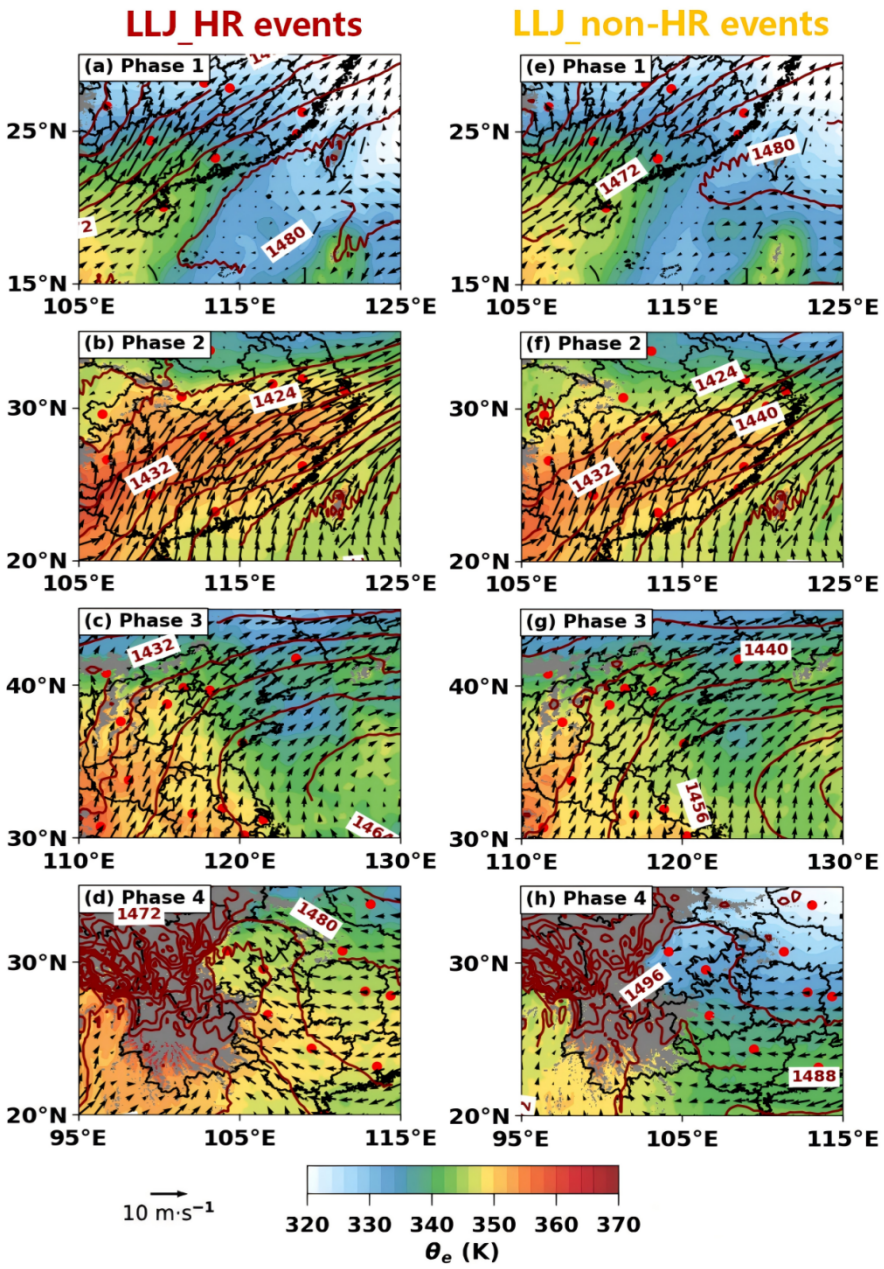

Figure 10. Distributions of equivalent potential temperature (shading, unit: K) at 850 hPa, superimposed with 850 hPa horizontal wind vectors (black arrows) and geopotential height contours (red solid lines), for LLJ_HR events within 1-hour time window preceding nocturnal rainfall onset in (a) ROI-1 during Phase 1, (b) ROI-2 during Phase 2, (c) ROI-3 during Phase 3, and (d) in ROI-4 during Phase 4. Gray shading denotes terrain elevation exceeding 850 hPa level. The reference vector (10 m s^{-1}) is shown at the lower-left corner. (e-h) Same as (a-d), but for LLJ_non-HR events

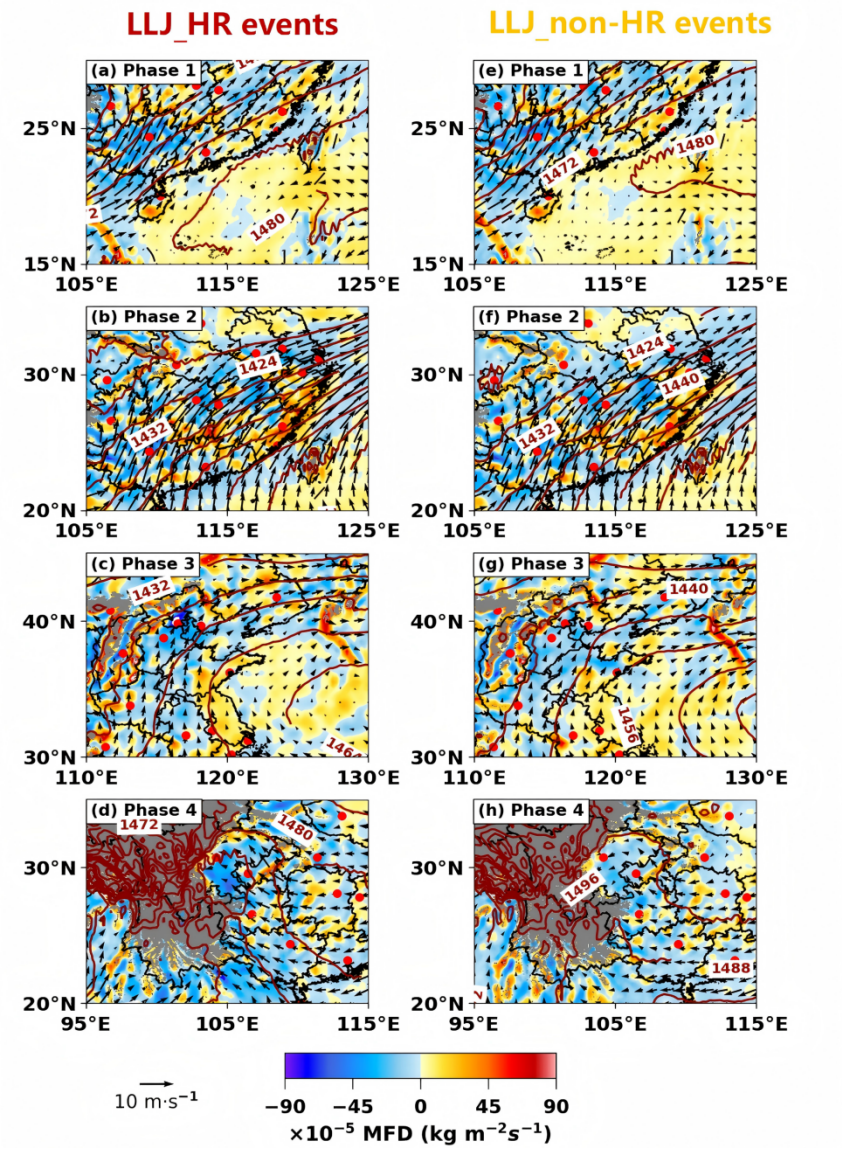

957

958 Figure 11. Same as Figure 10, but showing the integrated moisture flux divergence

959 (shading, unit: kg m^{-2} s^{-1}) between 1000–700 hPa at 1 hour prior to preceding

960 nocturnal rainfall onset

961

962

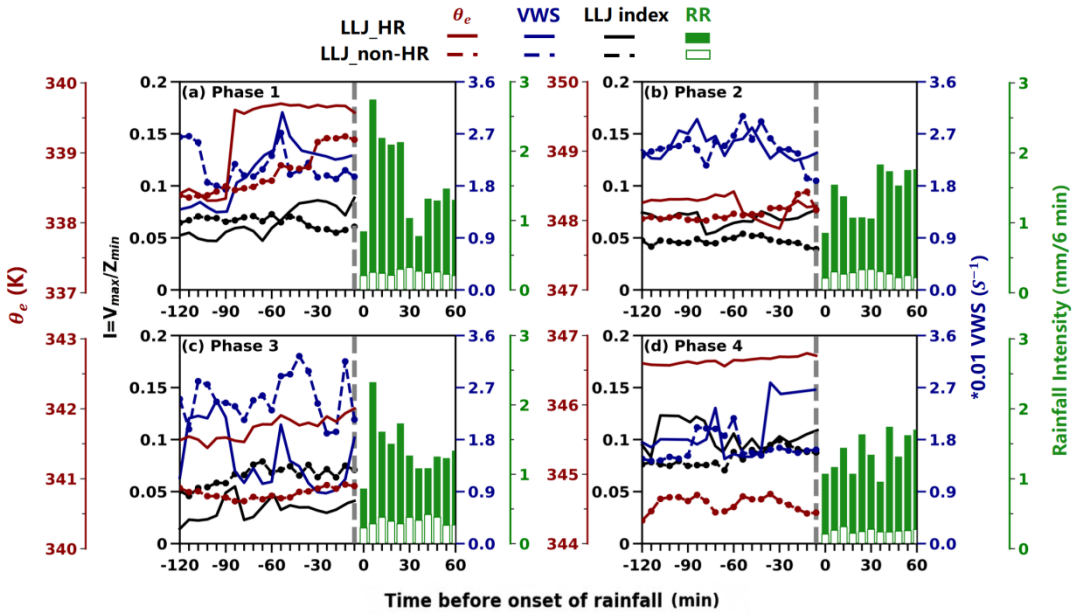

963

964 Figure 12. Temporal evolution of surface equivalent potential temperature (θ_e, red
965 lines), vertical wind shear (VWS, blue lines), and LLJ index (I, black lines) averaged
966 within 2 hours preceding nocturnal rainfall for LLJ_HR events (solid lines) and
967 LLJ_non-HR events (dashed lines) in (a) ROI-1 during Phase 1, (b) ROI-2 during Phase
968 2, (c) ROI-3 during Phase 3, and (d) in ROI-4 during Phase 4. Green bars denote 6-min
969 averaged rain rate (mm/ 6 min) after LLJ_HR (solid bars) and LLJ_non-HR (open bars)
970 events onset

971

972

973

974